

Ultrasound pulse-echo imaging using the split-step Fourier propagator

Lianjie Huang^a and Youli Quan^{a,b}

^aMail Stop D443, Los Alamos National Laboratory, Los Alamos, NM 87545

^bDepartment of Geophysics, Stanford University, Stanford, CA 94305

ABSTRACT

Ultrasonic reflection imaging has the potential to produce higher image resolution than transmission tomography, but imaging resolution and quality still need to be further improved for early cancer detection and diagnosis. We present an ultrasound reflection image reconstruction method using the split-step Fourier propagator. It is based on recursive inward continuation of ultrasonic wavefields in the frequency-space and frequency-wavenumber domains. The inward continuation within each extrapolation interval consists of two steps. In the first step, a phase-shift term is applied to the data in the frequency-wavenumber domain for propagation in a reference medium. The second step consists of applying another phase-shift term to data in the frequency-space domain to approximately compensate for ultrasonic scattering effects of heterogeneities within the breast. We use synthetic ultrasound pulse-echo data recorded around a ring for heterogeneous, computer-generated, numerical breast phantoms to study the imaging capability of the method. The phantoms are derived from an experimental breast phantom and a sound-speed tomography image of an *in-vivo* ultrasound breast data collected using a ring array. The heterogeneous sound-speed models used for pulse-echo imaging are obtained using a computationally efficient, first-arrival-time (time-of-flight) transmission tomography method. Our studies demonstrate that reflection image reconstruction using the split-step Fourier propagator with heterogeneous sound-speed models significantly improves image quality and resolution. We also numerically verify the spatial sampling criterion of wavefields for a ring transducer array.

Keywords: Image reconstruction, pulse-echo imaging, ring array, sampling criterion, split-step Fourier, transmission tomography, ultrasound breast imaging.

1. INTRODUCTION

Even though ultrasonic imaging is the second most often used imaging modality in medicine,¹ its role is usually limited to compliment the other major imaging modalities such as x-ray imaging. It is critical to significantly improve the image quality and resolution of ultrasonic imaging in order to make this imaging modality feasible for early breast cancer detection and diagnosis. Current limitations of ultrasonic imaging arise from commonly used linear transducer arrays that restrict the data acquisition aperture etc., and from the lack of compensation for ultrasonic scattering effects during image reconstruction, resulting in low-resolution and noisy images. To alleviate the first limitation, several groups have developed ring transducer arrays to increase the data acquisition aperture.²⁻⁹

The recent technological advances in ring transducer arrays provide an opportunity to accurately obtain sound-speed tomography images of the breast.¹⁰⁻¹³ Such images are normally smooth and the image resolution is low. In this paper, we present an ultrasound reflection image reconstruction method that makes use of smooth sound-speed tomography results for wavefield inward continuation to improve image quality and resolution. The wavefield extrapolation is carried out using the split-step Fourier propagator that has been used for modeling and imaging in other fields,¹⁴⁻¹⁸ but has not yet been studied for medical ultrasound imaging. We study the image reconstruction capability of the split-step Fourier propagator for ultrasound breast imaging using a ring array and computer-generated breast phantoms. The split-step Fourier propagator is based on the Fourier transform and phase shift in the frequency-wavenumber and frequency-space domains. Therefore, it minimizes the numerical dispersion and consequently reduces image artifacts. Reflection image reconstruction with the split-step Fourier propagator is computationally much more efficient than full wave-equation-based time-reversal image reconstruction,¹⁹ but more accurate than phase-shift image reconstruction.²⁰ We demonstrate that ultrasound reflection image reconstruction using the split-step Fourier propagator with heterogeneous sound-speed models significantly improves image resolution and quality compared to phase-shift image reconstruction.

Send correspondence to Lianjie Huang: ljh@lanl.gov

The sampling criterion of wavefields needed to image objects within a ring array has been developed recently.²¹ We use a synthetic ultrasound pulse-echo dataset recorded by a ring array for a computer-generated breast phantom to numerically verify the sampling criterion.

2. SPLIT-STEP FOURIER PROPAGATOR

The acoustic-wave equation can be decomposed into two one-way wave equations describing wave propagation in opposite directions. The one-way wave equation in the frequency-space domain is given by

$$\frac{\partial U(x, z; \omega)}{\partial z} = -i \sqrt{\frac{\omega^2}{v^2(x, z)} + \frac{\partial^2}{\partial x^2}} U(x, z; \omega) = -i Q(x, z; \omega) U(x, z; \omega), \quad (1)$$

where (x, z) is the space position, ω is the circular frequency, v is the sound speed, U is the acoustic wavefield, and the operator Q is defined by

$$Q(x, z; \omega) \equiv \sqrt{\frac{\omega^2}{v^2(x, z)} + \frac{\partial^2}{\partial x^2}} = \sqrt{\frac{\omega^2}{v_0^2(z)} + \frac{\partial^2}{\partial x^2}} + \left\{ \sqrt{\frac{\omega^2}{v^2(x, z)} + \frac{\partial^2}{\partial x^2}} - \sqrt{\frac{\omega^2}{v_0^2(z)} + \frac{\partial^2}{\partial x^2}} \right\} \quad (2)$$

with v_0 is a reference sound speed. Equation (2) can be approximated by

$$Q(x, z; \omega) \approx \sqrt{\frac{\omega^2}{v_0^2(z)} + \frac{\partial^2}{\partial x^2}} + \omega \left(\frac{1}{v(x, z)} - \frac{1}{v_0(z)} \right) = \sqrt{\frac{\omega^2}{v_0^2(z)} + \frac{\partial^2}{\partial x^2}} + \omega [s(x, z) - s_0(z)], \quad (3)$$

where the slowness $s = 1/v$, and the reference slowness $s_0 = 1/v_0$. The formal solution of equation (1) is

$$U(x, z + \Delta z; \omega) = \exp \left\{ -i \int Q dz \right\} U(x, z; \omega), \quad (4)$$

which extrapolates the acoustic wavefield U from z to $z + \Delta z$.

Inward continuation of the wavefield from receiving transducers into the breast using equation (4), together with equation (3), can be implemented with the following steps:

- (a) Fourier transform acoustic wavefield $U(x, z; \omega)$ with respect to x ;
- (b) Apply a phase-shift term $e^{-ik_z \Delta z}$ to the wavefield in the frequency-wavenumber $(\omega - k_x)$ domain, where $k_z = \sqrt{k_0^2 - k_x^2}$ with $k_0 = \omega/v_0$, and k_x is the wavenumber along the x -coordinate;
- (c) Inverse Fourier transform the resulting wavefield into the frequency-space $(\omega - x)$ domain;
- (d) Apply a phase-shift term $e^{-i\omega(s-s_0)}$ to approximately compensate for ultrasonic scattering effects of heterogeneities.

The resulting wavefield is the extrapolated acoustic wavefield. The wavefield inward continuation using the above procedure is termed the split-step Fourier (SSF) propagator.

For ultrasound pulse-echo signals, the ultrasound propagation time from a transmitter to a scatterer, and then back to the transmitter/receiver, is twice propagation time from the transmitter to the scatterer. Therefore, a time sample interval that is a half of that in pulse-echo data is used for pulse-echo imaging to focus scattering wavefields back to scatterers. The image $I(x, z)$ is obtained at time zero of backpropagated wavefields, and is calculated using

$$I(x, z) = \int U(x, z; \omega) d\omega. \quad (5)$$

One major advantage of the split-step Fourier method is that it is based on the Fourier transform, and therefore, the numerical dispersion is minimized. When using an assumption of uniform sound-speed for image reconstruction ($v = v_0$), the method leads to the phase-shift image reconstruction scheme.²⁰

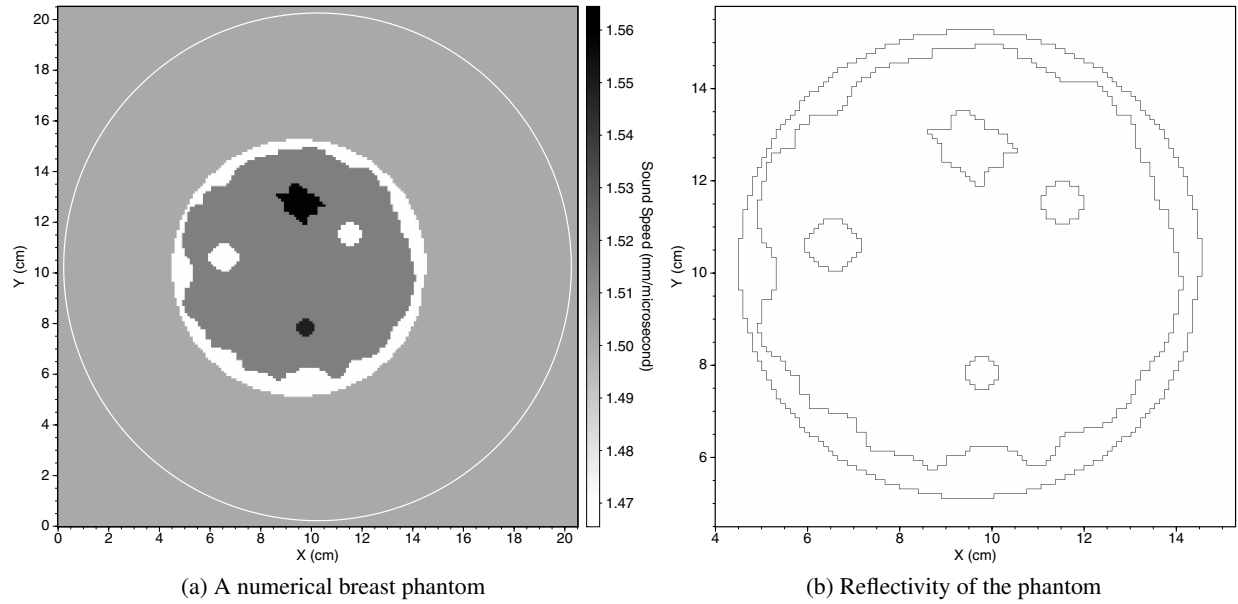


Figure 1: (a) Sound speed of a numerical breast phantom derived from an experimental breast phantom that contain two tumors with high sound-speeds, and two fatty tissues with low sound-speeds. The white solid circle in (a) is the ring array used to record synthetic pulse-echo data. (b) Reflectivity within the phantom in (a) shows where changes of acoustic impedances occur.

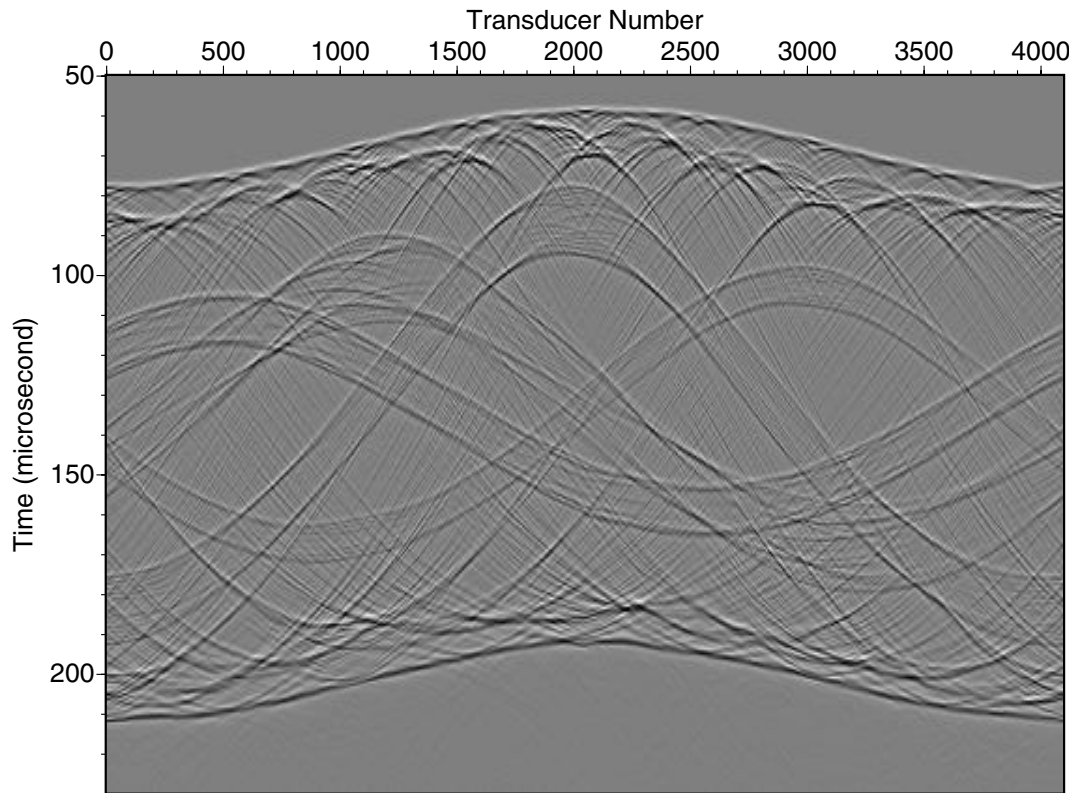


Figure 2: Computer-generated ultrasound pulse-echo data for the numerical breast phantom in Fig. 1(a). The central frequency of the data is 1 Mhz. The data clearly show scattering from the interfaces of the phantom tissues.

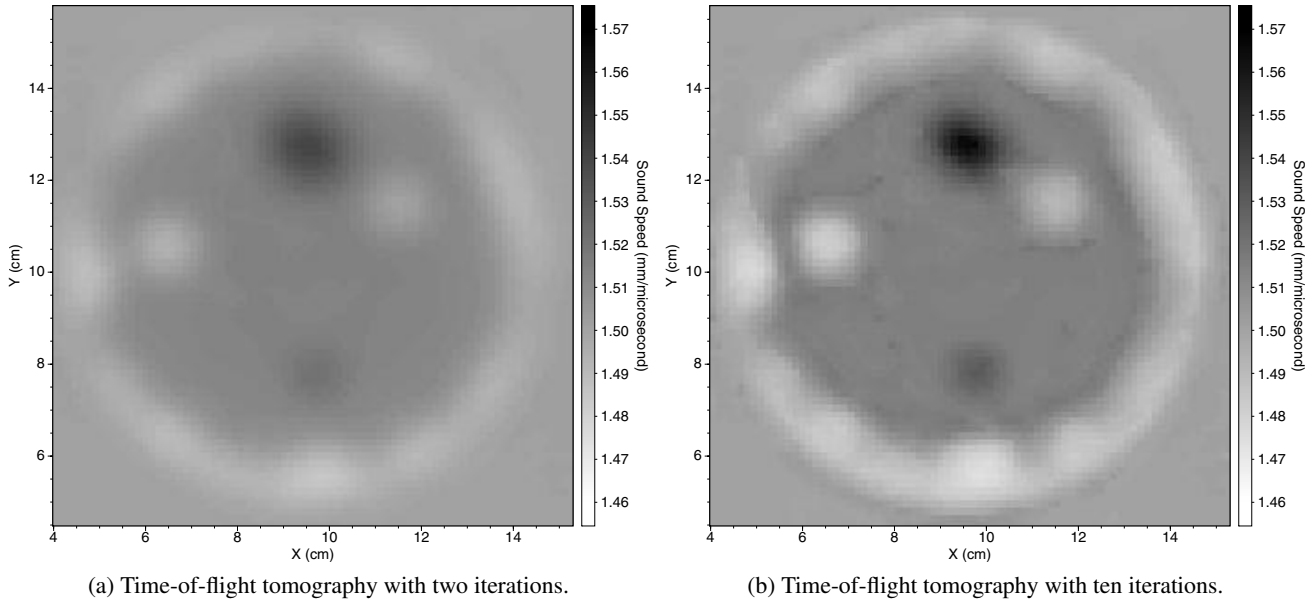


Figure 3: Time-of-flight sound-speed tomography results used for pulse-echo imaging for the numerical phantom in Fig. 1(a). The sound speed in (a) is a preliminary result obtained with only two iterations, and that in (b) is a more accurate one produced with ten iterations of the tomography inversion.

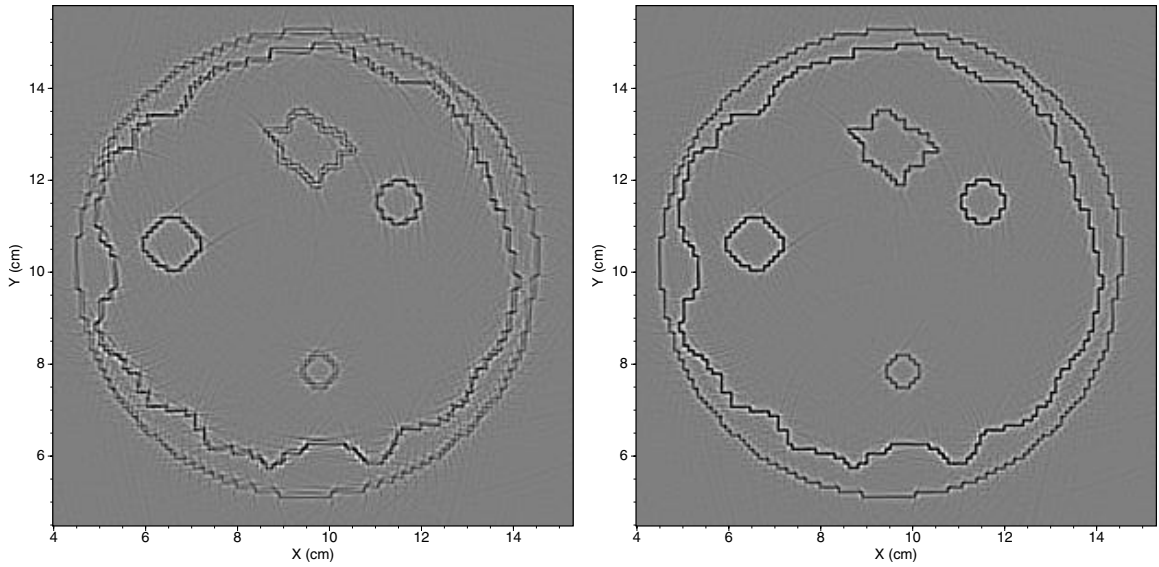
3. ULTRASOUND PULSE-ECHO IMAGING FOR A NUMERICAL PHANTOM DERIVED FROM AN EXPERIMENTAL BREAST PHANTOM

Two numerical breast phantoms are used to investigate the capability of the split-step Fourier propagator for reflection image reconstruction. An important advantage of using computer-generated phantoms in image-reconstruction studies is that the exact sound-speed model of the phantoms is known, and thus the reflection image reconstructed using the exact sound-speed provides a gold standard of image quality and resolution that could be achieved using a given image-reconstruction algorithm. Another advantage is that numerical phantoms can be easily altered to simulate different anatomies and medical situations. It is difficult to study combinations of different medical situations of patients using clinical data.

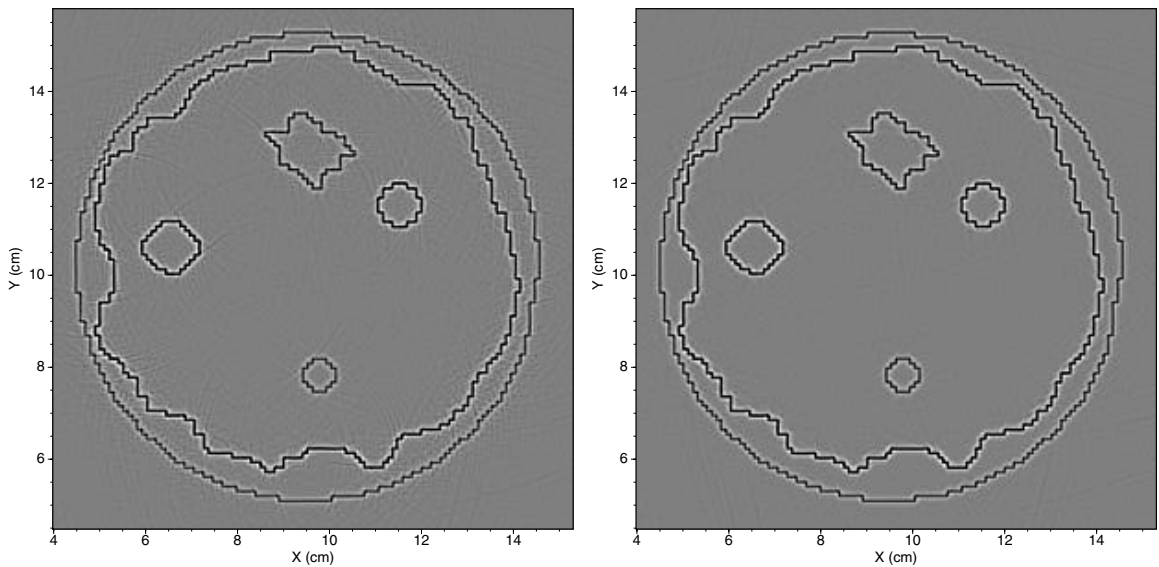
The first numerical breast phantom, shown in Fig. 1(a), contains four phantom breast masses. It is derived from an experimental breast phantom at Karmanos Cancer Institute. It consists of a subcutaneous layer of fat, a faceted parenchyma, and two tumors with higher sound speeds and two fatty masses with lower sound speeds compared to the surrounding tissue. The larger tumor is more irregular than the other anomalies. The surfaces of all phantom breast masses in Fig. 1(a) are rough, resulting in a significant amount of ultrasound scattering. An enlarged display of reflectivity (normal reflection coefficient) within the phantom is given in Fig. 1(b). The maximum value of reflectivity is 0.015. It would be ideal if reflection images would look like the reflectivity.

We use a finite-difference time-domain scheme for the acoustic-wave equation in heterogeneous media to generate ultrasound pulse-echo data for the numerical breast phantom in Fig. 1(a). We assume that the densities of the phantom tissues are proportional to their sound speeds during the finite-difference calculation. The data are recorded at 4096 transducers that are equally distributed around the ring shown as the white solid circle in Fig. 1(a). The central frequency of the data is 1 MHz. The ring array has a diameter of 20 cm. Each transducer receives scattering signals emitted from itself. The synthetic pulse-echo data in Fig. 2 clearly show ultrasonic scattering from the interfaces of four anomalies, in addition to other scattering signals.

Image reconstruction with the split-step Fourier propagator requires a heterogeneous sound-speed model. We obtain the heterogeneous sound-speed models of the numerical breast phantom using a time-of-flight transmission tomography method,¹³ in which transmission ultrasound data are used instead of pulse-echo data. This tomography method is computationally efficient, particularly when only using a few iterations in tomography inversion to produce a reasonably accurate sound-speed image. Two time-of-flight transmission tomography results for the phantom in Fig. 1(a) are shown in Figs. 3(a)



(a) Phase-shift reconstruction with a uniform sound-speed. (b) SSF reconstruction with a sound-speed model in Fig. 3(a).



(c) SSF reconstruction with a sound-speed model in Fig. 3(b). (d) SSF reconstruction with the phantom sound-speed in Fig. 1(a).

Figure 4: Comparison of ultrasound pulse-echo imaging using the split-step Fourier propagator with different sound-speed models. Image reconstructions with heterogeneous sound-speed models in (b)-(d) significantly improve image quality and resolution compared with that obtained using a uniform sound-speed in (a).

and (b), where the sound speed in (a) is a preliminary result obtained with only two iterations, and that in (b) is a more accurate one with ten iterations. It takes less than 20 seconds on a desktop computer to obtain the preliminary result in Fig. 3(a).

We conduct ultrasound pulse-echo imaging with the split-step Fourier propagator using the synthetic pulse-echo data in Fig. 2. In the image reconstructions, four different sound-speed models are used: a uniform one obtained using the average slowness of the numerical breast phantom (Fig. 1a), two time-of-flight sound-speed tomography results, as shown in Figs. 3 (a) and (b), and the original (correct) sound-speed model of the phantom shown in Fig. 1(a). Figure 4 shows

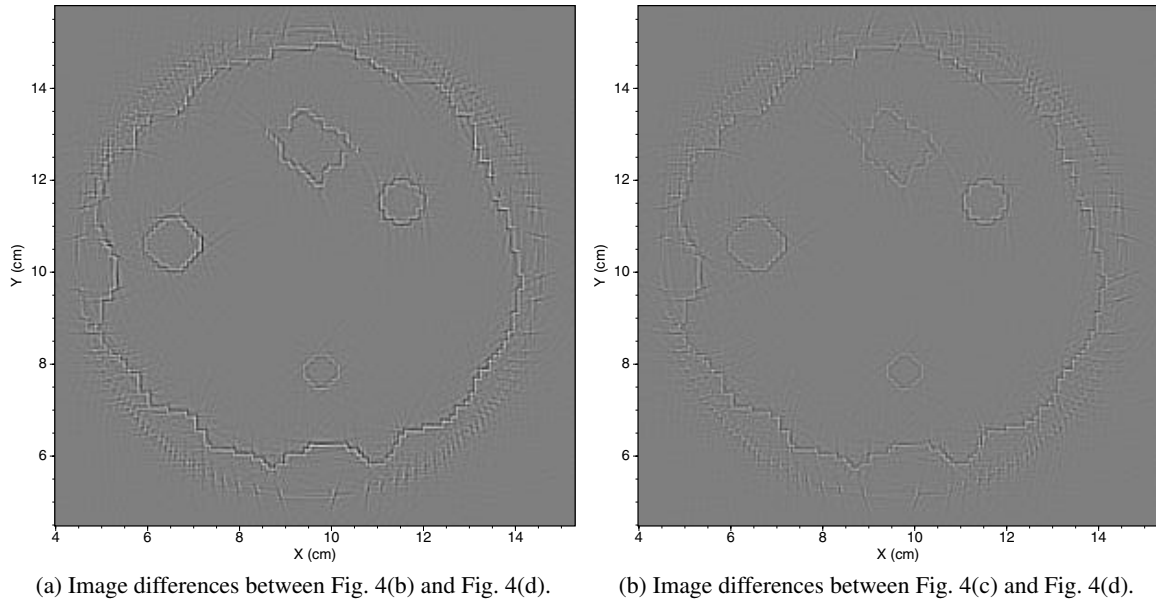


Figure 5: Differences of images between those obtained using sound-speed tomography results and that yielded using the original (correct) phantom sound speed. The differences in (b) are smaller than those in (a). The image differences are plotted using the same scale as that in Fig. 4(d).

a comparison of the reconstructed reflection images. As depicted in Fig. 4(a), the phase-shift image reconstruction using a uniform sound-speed model produced a blurred image with significant artifacts. When even only using a preliminary tomography result (Fig. 3a) for SSF image reconstruction (Fig. 4b), the image resolution is significantly improved, and the image contains fewer artifacts than the phase-shift image reconstruction (Fig. 4a). As demonstrated in Figs. 4(b) and (c), imaging quality is further improved using the more accurate sound-speed tomography result shown in Fig. 3(b), and is the best when using the original sound-speed of the phantom (Fig. 1a) for image reconstruction (Fig. 4d). Figure 4(d) contains fewer image artifacts than Figs. 4(a)-(c), but no exact sound-speed model will be available in practice. Nevertheless, the images in Figs. 4(b)-(d) are similar to the reflectivity depicted in Fig. 1(b).

To compare image differences more clearly, Fig. 5 shows the image differences between Fig. 4(b) and Fig. 4(d), and those between Fig. 4(c) and Fig. 4(d). We can see that the image differences decrease with increasing accuracy of sound-speed tomography results, or the image quality and resolution improve with increasing accuracy of the sound-speed models used for image reconstruction.

4. ULTRASOUND PULSE-ECHO IMAGING FOR A NUMERICAL PHANTOM DERIVED FROM AN *IN-VIVO* SOUND-SPEED TOMOGRAPHY IMAGE

Another numerical breast phantom we used to test the capability of the split-step Fourier propagator for image reconstruction is derived from sound-speed tomography image of an *in-vivo* ultrasound breast dataset, collected using Karmanos Cancer Institute's ring transducer array.⁹ We obtain the sound-speed image from the data using a time-of-flight transmission tomography method.¹³ We then derive a numerical breast phantom from the sound-speed tomography image by removing the tomography artifacts. The phantom is depicted in Fig. 6(a). The low sound-speed regions in the phantom represent fatty tissues, and the high sound-speed region is a breast cancer. Fig. 6(b) is an enlarged display of reflectivity (normal reflection coefficient) within the phantom, showing the gold standard of reflection image reconstruction. The maximum value of the reflectivity is 0.0001639, that is two orders of magnitude smaller than that of the phantom in Fig. 1(a).

We use again a finite-difference time-domain acoustic-wave equation scheme to compute ultrasound pulse-echo data for the numerical breast phantom in Fig. 6(a). We assume that the densities of the phantom tissues are proportional to their sound speeds during the finite-difference modeling. Figure 7 is the synthetic data recorded at 4096 transducers equally distributed around the ring shown as the white solid circle in Fig. 6(a). The central frequency of the data is 1 MHz and the ring array has a diameter of 20 cm.

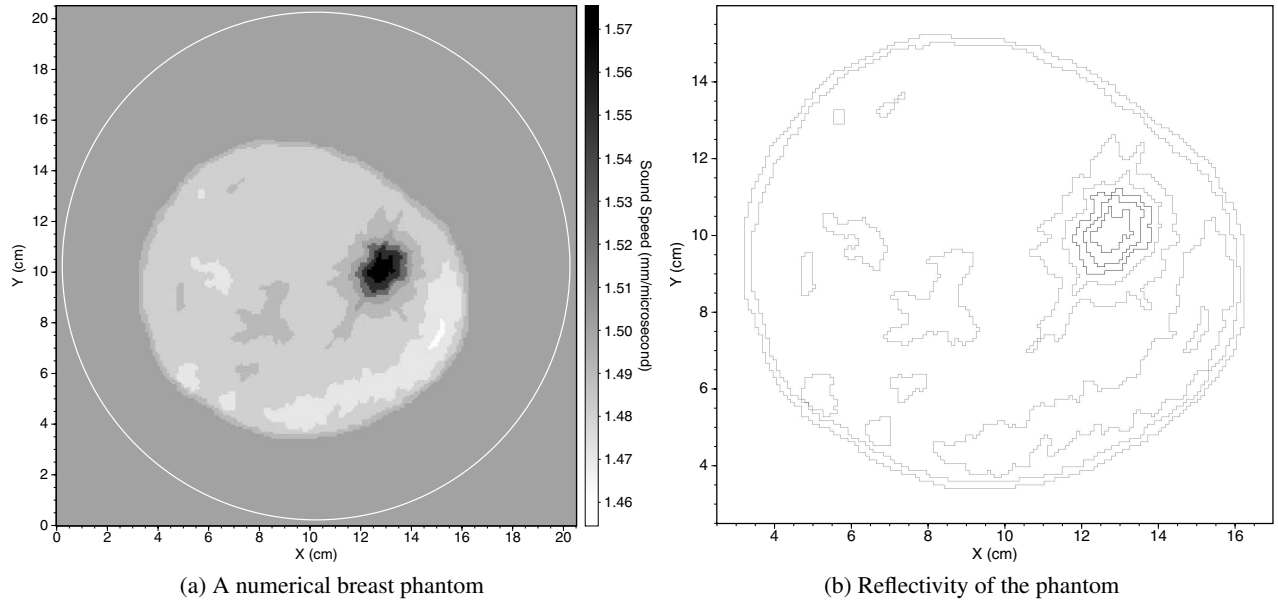


Figure 6: (a) Sound speed of a numerical breast phantom derived from a sound-speed tomography result of an *in-vivo* ultrasound breast data. The phantom contains heterogeneous breast tissues and a breast cancer with a higher sound speed than its surrounding tissues. The white solid circle in (a) is the ring array used to record synthetic pulse-echo data. (b) Reflectivity within the phantom in (a) shows where changes of acoustic impedances occur.

Figures 8(a) and (b) are, respectively, results from two and ten iterations of the time-of-flight transmission tomography inversion for the numerical breast phantom in Fig. 6(a).¹³ Figure 8(b) is a more accurate sound-speed model than Fig. 8(a). We use these sound-speed models to reconstruct reflection images using the split-step Fourier propagator and the synthetic pulse-echo data in Fig. 7. For comparison, we also carry out ultrasound pulse-echo imaging using the phase-shift method with a uniform sound-speed model, and split-step Fourier image reconstruction with the correct phantom sound-speed. The reconstructed images are shown in Fig. 9, demonstrating once again that image quality and resolution are greatly enhanced by using a reasonably accurate sound-speed models for image reconstruction. The images in Fig. 9(b)-(d) match very well with the reflectivity of the phantom as shown in Fig. 6(b).

Figure 10(a) shows the image differences between Fig. 9(b) and Fig. 9(d), and Fig. 10(b) depicts the differences between Fig. 9(c) and Fig. 9(d). Figure 10 shows that the image differences decrease with increasing accuracy of sound-speed tomography results used for image reconstruction. Practically, image reconstruction using a sound-speed tomography result with five to ten iterations of the tomography inversion can produce high-quality and high-resolution reflection images.

5. NUMERICAL VERIFICATION OF THE SAMPLING CRITERION OF WAVEFIELDS FOR A RING ARRAY

The sampling criterion of wavefields needed to image objects within a ring array has recently been developed²¹ and is given by

$$\Delta < \frac{\lambda R}{2r_0}, \quad (6)$$

where Δ is the transducer spatial interval, λ is the wavelength, R is the radius of the ring array, and r_0 is radius of the object to be imaged.

In our image reconstruction studies using the numerical breast phantom in Fig. 6(a) and the pulse-echo data in Fig. 7, $\lambda \approx 1.5$ mm, $R = 100$ mm, $r_0 \approx 60$ mm. Therefore, the transducer interval must satisfy $\Delta < 1.25$ mm according to equation (6).

We conduct the split-step Fourier image reconstruction using 2048, 1024, 512, and 256 transducers recording ultrasound pulse-echo data as shown in Fig. 7, and the reflection image reconstruction results are shown in Fig. 11. The

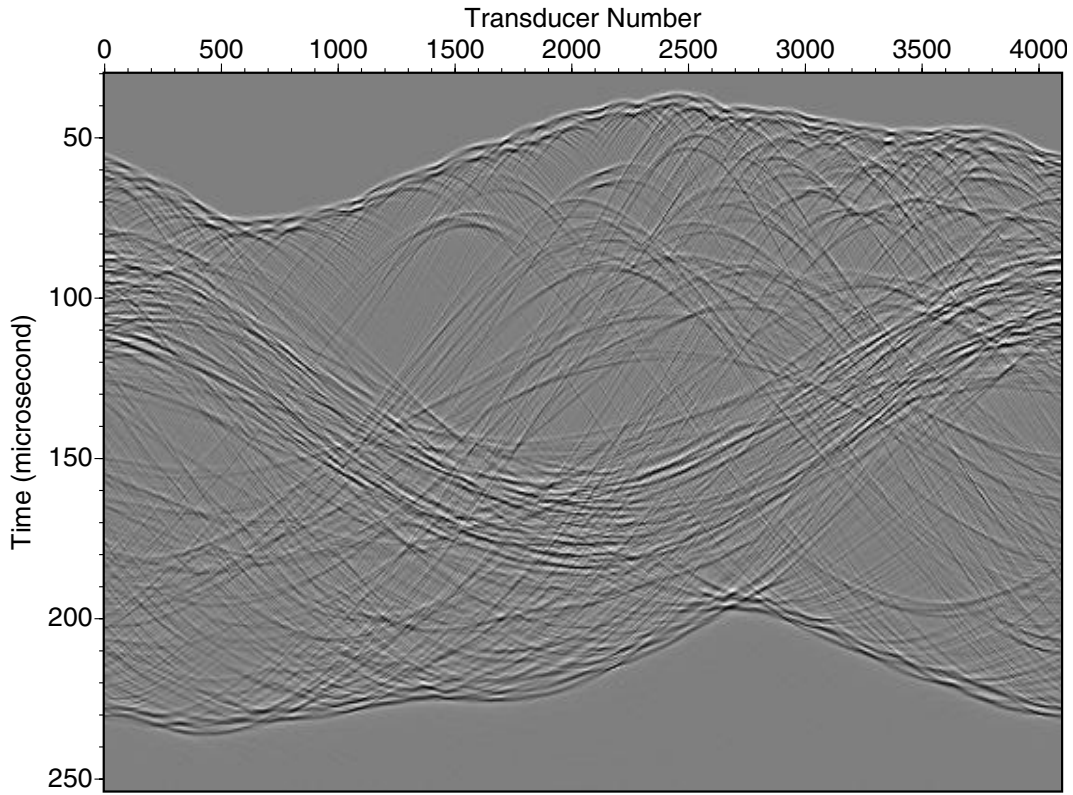


Figure 7: Computer-generated ultrasound pulse-echo data for the numerical breast phantom in Fig. 6(a). The central frequency of the data is 1 MHz. The data show ultrasonic scattering from the heterogeneous phantom tissues.

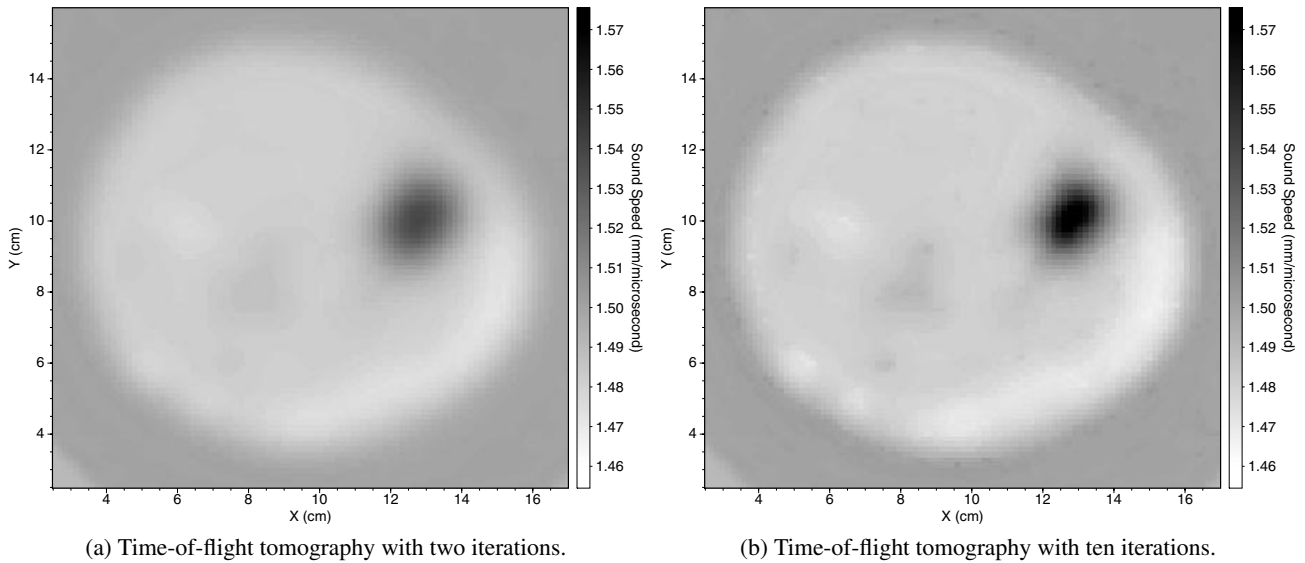
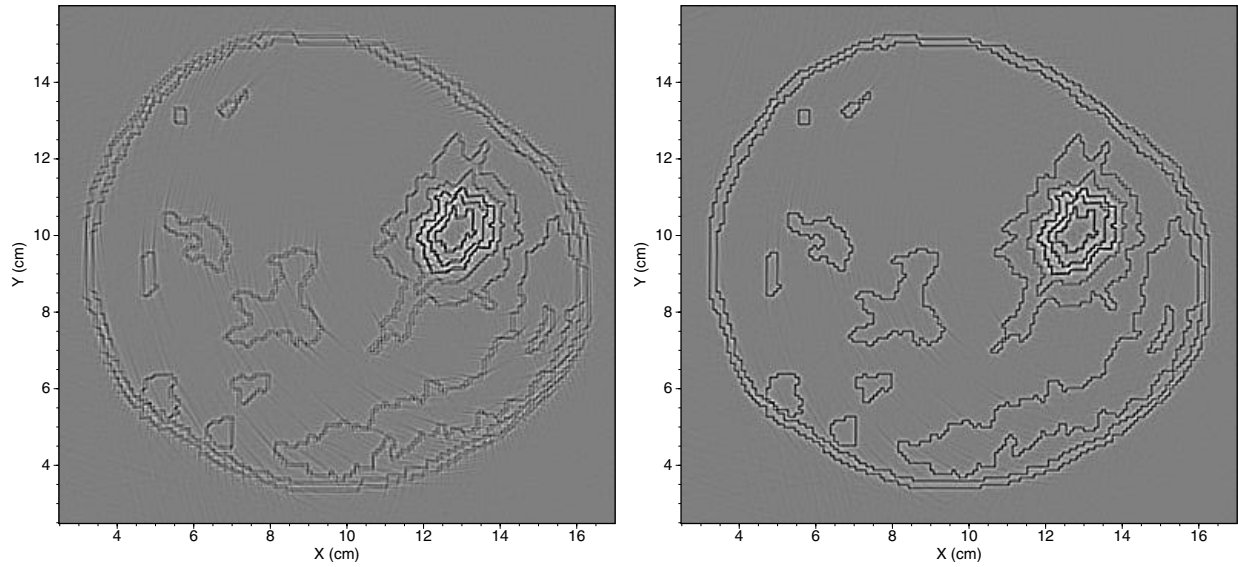
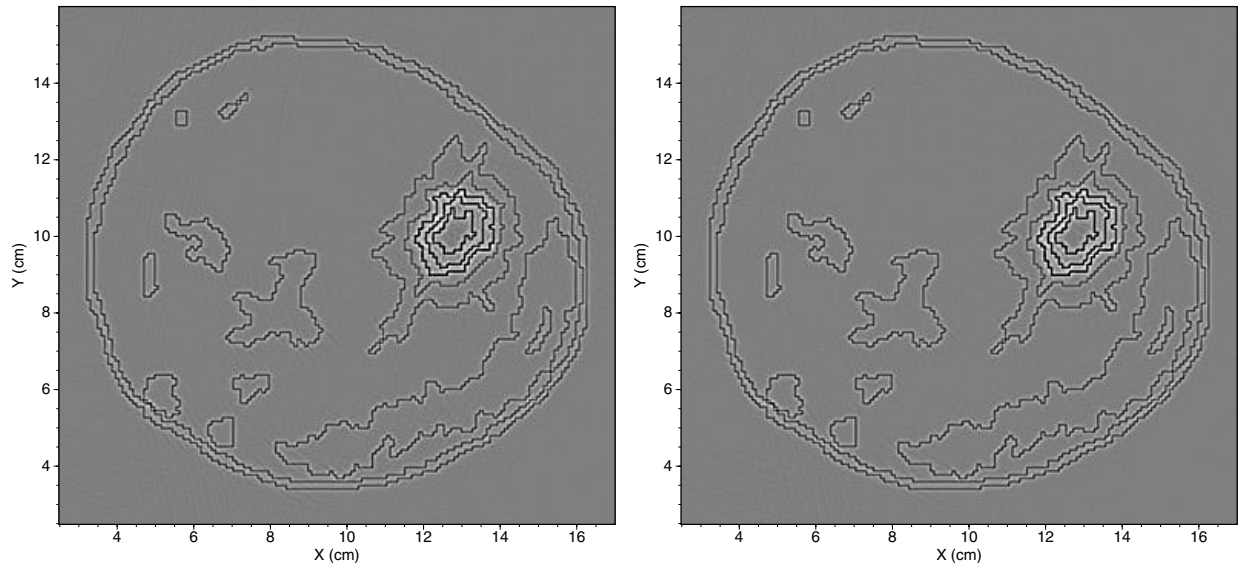


Figure 8: Time-of-flight sound-speed tomography results used for pulse-echo imaging for the numerical phantom in Fig. 6(a). The preliminary result in (a) is generated with two iterations, and the result in (b) is a more accurate one yielded with ten iterations of the tomography inversion.



(a) Phase-shift reconstruction with a uniform sound-speed.

(b) SSF reconstruction with a sound-speed model in Fig. 8(a).



(c) SSF reconstruction with a sound-speed model in Fig. 8(b)

(d) SSF reconstruction with the phantom sound-speed in Fig. 6(a).

Figure 9: Comparison of ultrasound pulse-echo imaging using the split-step Fourier propagator with different sound-speed models. Image reconstructions with heterogeneous sound-speed models in (b)-(d) significantly improve image quality and resolution compared with that obtained using a uniform sound-speed in (a).

corresponding transducer intervals are 0.31 mm, 0.61 mm, 1.23 mm, and 2.45 mm, respectively. The sound-speed tomography model depicted in Fig. 8(b) is used for the image reconstruction. The transducer intervals for Figs. 11(a)-(c) satisfy the sampling criterion of wavefields for the ring array, but that for Figs. 11(d) does not, leading to significant image artifacts inside and outside the phantom area. Even though Fig. 11(c) contains some image artifacts outside the phantom region, the image within the phantom has significantly fewer artifacts than that in Fig. 11(d).

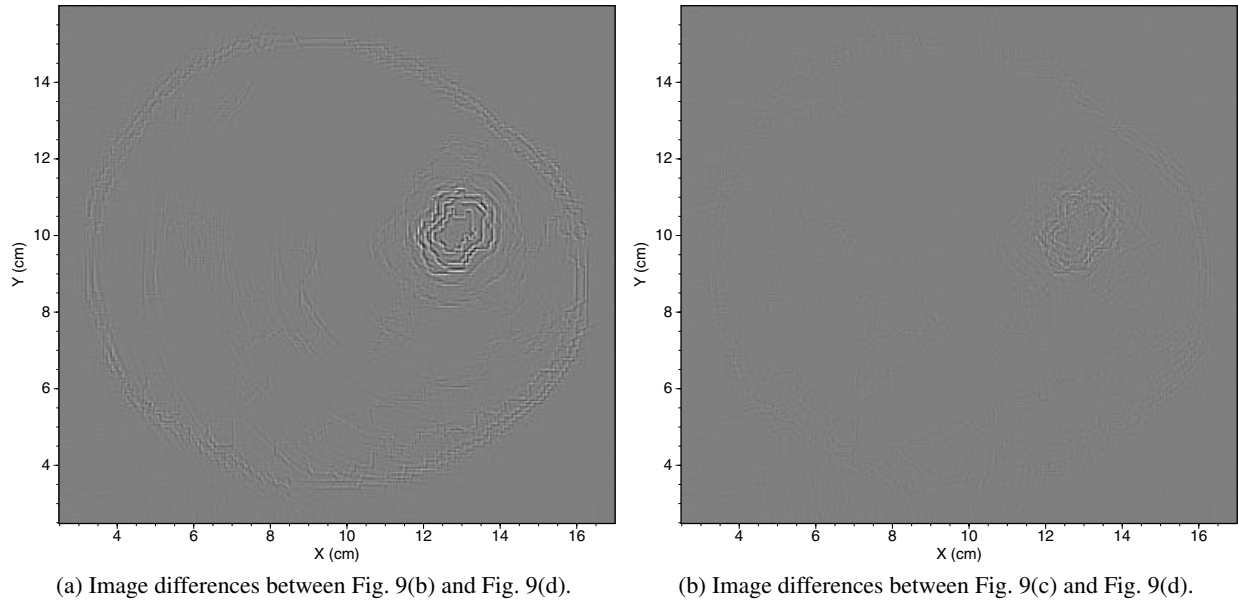


Figure 10: Differences of images between those obtained using sound-speed tomography results and that produced using the original (correct) phantom sound-speed. The differences in (b) is smaller than that in (a). The image differences are plotted using the same scale as that in Fig. 9(d).

6. CONCLUSIONS

We have studied an ultrasound pulse-echo imaging method using the split-step Fourier propagator. The method uses heterogeneous sound-speed models obtained from time-of-flight transmission tomography for image reconstruction to approximately compensate for ultrasonic scattering effects. We have investigated the capability of the method for reflection image reconstruction using two different numerical breast phantoms and synthetic pulse-echo data recorded by a ring array. We have demonstrated that image reconstruction with the split-step Fourier propagator and a heterogeneous sound-speed model significantly improves image resolution and quality, even when using only a preliminary estimate of the sound speed. We have also numerically verified the spatial sampling criterion of wavefields for a ring array.

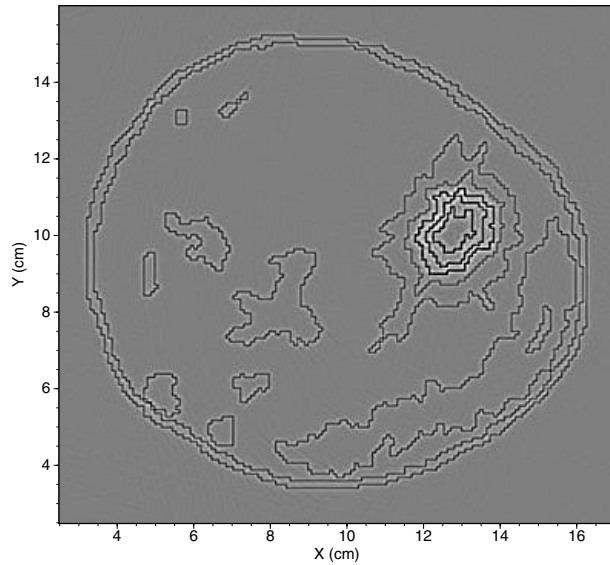
Waveform tomography has the potential to produce higher-resolution sound-speed images than time-of-flight transmission tomography.²² We will study to use sound-speed models obtained using waveform tomography for ultrasound reflection image reconstruction to further improve image quality and resolution. In addition, we will study the capability of the ultrasound reflection image reconstruction with the split-step Fourier propagator for more realistic and complex numerical breast phantoms, and apply the method to *in-vivo* ultrasound breast data collected using a ring array.

ACKNOWLEDGMENTS

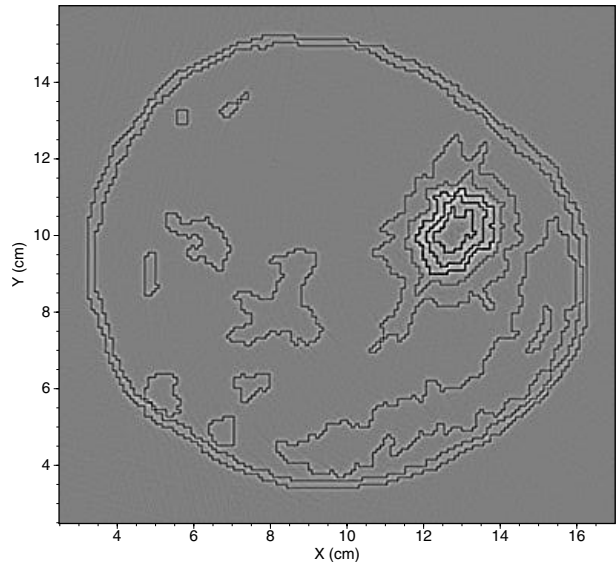
This work was supported through the U.S. DOE Laboratory-Directed Research and Development program at Los Alamos National Laboratory. The numerical breast phantoms were derived from a breast phantom and a clinic breast tomography image provided by Karmanos Cancer Institute through Neb Duric. We thank Kenneth Hanson and Douglas Alde of Los Alamos National Laboratory for reviewing the paper.

REFERENCES

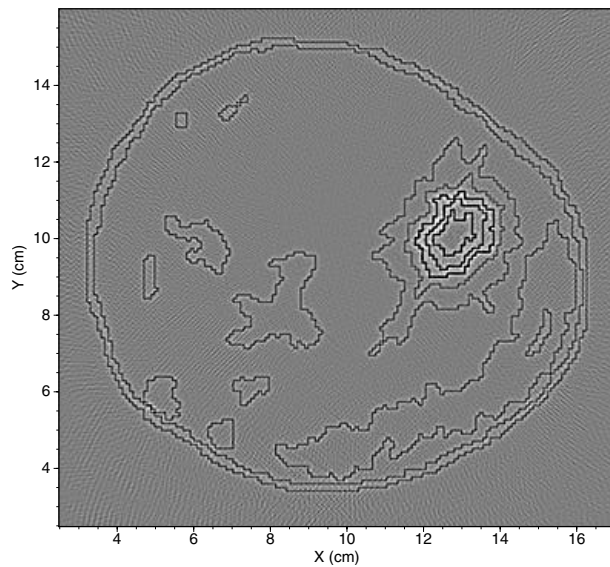
1. S. Hughes, "Medical ultrasound imaging," *Physics Education*, pp. 468–475, 2001.
2. S. J. Norton and M. Linzer, "Ultrasonic reflectivity tomography: reconstruction with circular transducer arrays," *Ultrasonic Imaging* **2**, pp. 154–184, 1979.
3. J. S. Schreiman, J. J. Gisvold, J. F. Greenleaf, and R. C. Bahn, "Ultrasound transmission computed tomography of the breast," *Radiology* **150**, pp. 523–530, 1984.



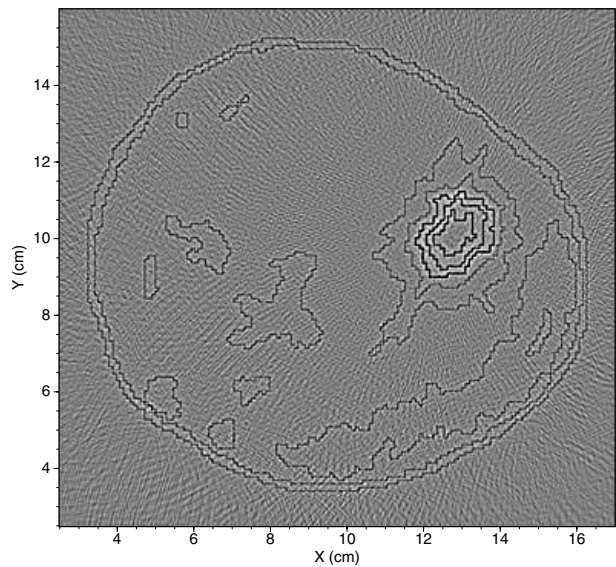
(a) Image reconstruction using a ring array with 2048 transducers.



(b) Image reconstruction using a ring array with 1024 transducers.



(c) Image reconstruction using a ring array with 512 transducers.



(d) Image reconstruction using a ring array with 256 transducers.

Figure 11: Ultrasound pulse-echo imaging results for the numerical breast phantom in Fig. 6(a) with different numbers of transducers in the ring array. The sound speed used for image reconstruction is that in Fig. 8(b). The imaging quality decreases significantly when the number of transducers is less than 512, or when the transducer spacing violates the sampling criterion for the ring array.

4. P. J. Littrup, N. Duric, S. Azevedo, D. H. Chambers, J. V. Candy, S. Johnson, G. Auner, J. Rather, and E. T. Holsapple, "Computerized Ultrasound Risk Evaluation (CURE) system: Development of combined transmission and reflection ultrasound with new reconstruction algorithms for breast imaging," *Acoustical Imaging* **26**, pp. 175–182, 2002.
5. R. Stotzka, G. Gobel, and K. Schlote-Holubek, "Development of transducer arrays for ultrasound-computertomography," in *Ultrasonic Imaging and Signal Processing*, W. F. Walker and M. Insana, eds., *Proc. SPIE Medical Imaging* **5035**, pp. 513–520, 2003.
6. N. Duric, P. J. Littrup, O. Rama, and E. T. Holsapple, "Computerized ultrasound risk evaluation (CURE): First clinical

- results,” *Acoustical Imaging* **28**, 2005.
7. S. A. Johnson, D. T. Borup, J. W. Wiskin, m Berggren, B. H. anf F Setinsek, S. Olsen, and K. Callahan, “From laboratory to clinical trials: An odyssey of ultrasound inverse scattering imagging for breast cancer diagnosis,” *J. Acoust. Soc. Am.* **120**, p. 3023, 2006.
 8. R. C. Waag and R. J. Fedewa, “A ring transducer system for medical ultrasound research,” *IEEE Transactions on Ultrasonics, Ferroelectrice, and Frequency Control* **53**, pp. 1707–1718, 2006.
 9. N. Duric, P. Littrup, L. Poulo, A. Babkin, R. Pevzner, E. Holsapple, and O. Rama, “Detection of breast cancer with ultrasound tomography: First results with the computerized ultrasound risk evaluation (c.u.r.e) prototype,” *Medical Physics* **32**, 2007 (accepted).
 10. M. P. Andre, H. S. Janee, P. J. Martin, G. P. Otto, B. A. Spivey, and D. A. Palmer, “High-speed data acquisition in a diffraction tomography system employing large-scale toroidal arrays,” *International Journal of Imaging Systems and Technology* **8**, pp. 137–147, 1997.
 11. D. H. Chambers and P. Littrup, “Ultrasound imaging using diffraction tomography in a cylindrical geometry,” in *Ultrasonic Imaging and Signal Processing*, M. Insana and W. F. Walker, eds., *Proc. SPIE Medical Imaging* **4687**, pp. 412–420, 2002.
 12. N. Duric, P. Littrup, E. T. Holsapple, A. Babkin, R. Duncan, A. Kalinin, R. Pevzner, and M. Tokarev, “Ultrasound tomography of breast tissue,” in *Ultrasonic Imaging and Signal Processing*, W. F. Walker and M. Insana, eds., *Proc. SPIE Medical Imaging* **5035**, 2003.
 13. Y. Quan and L. Huang, “Sound-speed tomography using first-arrival transmission ultrasound for a ring array,” in *Ultrasonic Imaging and Signal Processing*, S. Y. Emelianov and S. A. McAleavey, eds., *Proc. SPIE Medical Imaging* **6513**, 2007.
 14. R. H. Hardin and F. D. Tappert, “Applications of the split-step Fourier method to the numerical solution of the nonlinear and variable coefficient wave equations,” *SIAM Rev.* **15**, p. 423, 1973.
 15. F. D. Tappert, “The parabolic approximation method,” in *Wave Propagation in Underwater Acoustics*, J. B. Keller and J. S. Papadakis, eds., pp. 224–287, 1977.
 16. P. L. Stoffa, J. T. Fokkema, R. M. de Luna Freire, and W. P. Kessinger, “Split-step Fourier migration,” *Geophysics* **55**, pp. 410–421, 1990.
 17. L. Huang and M. C. Fehler, “Accuracy analysis of the split-step Fourier propagator: implications for seismic modeling and migration,” *Bull. Seis. Soc. Am.* **88**, pp. 18–29, 1998.
 18. F. B. Jensen, W. A. Kuperman, M. B. Porter, and H. Schmidt, *Computational Ocean Acoustics*, Springer-Verlag, New York, 2000.
 19. L. Huang, N. Duric, and P. Littrup, “Breast imaging with time-reversed ultrasound,” in *Ultrasonic Imaging and Signal Processing*, S. Emelianov and W. F. Walker, eds., *Proc. SPIE Medical Imaging* **6147**, pp. 156–167, 2006.
 20. L. Huang, N. Duric, and P. Littrup, “Ultrasonic breast imaging using a wave-equation migration method,” in *Ultrasonic Imaging and Signal Processing*, W. F. Walker and M. Insana, eds., *Proc. SPIE Medical Imaging* **5035**, pp. 432–439, 2003.
 21. F. Simonetti, L. Huang, and N. Duric, “On the spatial sampling of wave fields with circular ring apertures,” *Journal of Applied Physics* , 2007 (accepted).
 22. R. G. Pratt, L. Huang, N. Duric, and P. Littrup, “Sound-speed and attenuation of the breast tissue using waveform tomography of transmission ultrasound data,” in *Physics of Medical Imaging*, J. Hsieh and M. J. Flynn, eds., *Proc. SPIE Medical Imaging* **6510**, 2007.